On the role of the actin cytoskeleton and nucleus in the biomechanical response of spread cells

On the role of the actin cytoskeleton and nucleus in the biomechanical response of spread cells

N.H. Reynolds[1,2], W. Ronan[1], E.P. Dowling[1], P. Owens[3], R.M. McMeeking[4], *J.P. McGarry[1,2]

Affiliations

1. College of Engineering and Informatics, National University of Ireland Galway

2. National Centre for Biomedical Engineering Science, National University of Ireland Galway

3. Centre for Microscopy and Imaging, National University of Ireland Galway

4. Department of Mechanical Engineering, University of California, Santa Barbara, USA

Corresponding Author:

E-mail: *patrick.mcgarry@nuigalway.ie

Tel: +353 91 493165

Abstract

Micropipette aspiration (MA) has been used extensively in biomechanical investigations of un-adhered cells suspended in media. In the current study, a custom MA system is developed to aspirate substrate adhered spread cells. Additionally, the system facilitates immuno-fluorescent staining of aspirated cells to investigate stress fibre redistribution and nucleus deformation during MA. In response to an applied pressure, significantly lower aspiration length is observed for untreated contractile cells compared to cells in which actin polymerisation is chemically inhibited, demonstrating the important contribution of stress fibres in the biomechanical behaviour of spread cells. Additional experiments are performed in which untreated contractile cells are subjected to a range of applied pressures. Computational finite element simulations reveal that a viscoelastic material model for the cell cytoplasm is incapable of accurately predicting the observed aspiration length over the range of applied pressures. It is demonstrated that an active computational framework that incorporates stress fibre remodelling and contractility must be used in order to accurately simulate MA of untreated spread cells. Additionally, the stress fibre distribution observed in immuno-fluorescent experimental images of aspirated cells is accurately predicted using the active stress fibre modelling framework. Finally, a detailed experimental-computational investigation of the nucleus mechanical behaviour demonstrates that the nucleus is highly deformable *in cyto*, reaching strain levels in excess of 100% during MA. The characterisation of stress fibres and nucleus biomechanics in spread cells presented in the current study can potentially be used to guide tissue engineering strategies to control cell behaviour and gene expression.

Keywords: micropipette aspiration; actin cytoskeleton; nucleus; in vitro test; modelling; mechanical properties.

1 Introduction

The micropipette aspiration (MA) technique is used extensively to study the mechanical behaviour of single cells [1]. However, primarily due to the technical complexity of performing MA on cells adhered to a substrate or extra cellular matrix (ECM), the MA technique has largely been limited to the investigation of un-adhered cells suspended in media. Previous experimental MA studies have focused on suspended endothelial cells [2-4], suspended chondrocytes [5-7], suspended stem cells [8], and suspended fibroblasts [9]. Critically, in suspended cells a fibrillous contractile actin cytoskeleton is not developed [2, 10]. In contrast, cells adhered to a substrate or ECM develop a highly structured contractile actin cytoskeleton [11-13]. Therefore, the study of un-adhered suspended cells provides limited insight into the behaviour of contractile cells. The development of a robust MA system to investigate the biomechanical behaviour of spread adhered cells, with emphasis on the contribution of the actin cytoskeleton, would represent a significant advance in the field of experimental cell mechanics.

Previous studies have assumed simple viscoelastic constitutive behaviour for cells in order to interpret MA experimental data [3, 14]. However, such material models fail to consider the underlying biomechanisms of cell response to mechanical stimuli and a number of studies have demonstrated that passive material model parameters must be artificially altered if any experimental parameter is altered [15, 16], i.e. a unique set of passive material properties cannot be identified for a cell. The significant contribution of the actin cytoskeleton to the mechanical response of cells has been demonstrated in numerous experimental studies [17, 18]. It has recently been demonstrated that a computational cell model must include the key features of remodelling and contractility of the actin cytoskeleton in order to provide a realistic prediction of cell biomechanical response to physical stimuli [18-22]. Such advanced modelling techniques have not previously been applied to the simulation of MA of cells. The incorporation of the key bio-chemo-mechanical features of actin cytoskeleton remodelling and contractility should be of particular importance to the modelling of MA of spread adhered cells which contain a highly developed network of actin stress fibres (SFs).

Significantly advancing on the previous studies of suspended cells, the current study develops an experimental technique for the MA of spread adhered cells. In particular, the important role of the actin cytoskeleton is investigated, both in terms of its contribution to the mechanical response of the cell, and in terms of its redistribution in the cytoplasm during MA. Importantly, it is demonstrated that passive viscoelastic models do not provide an accurate prediction of the observed response of spread cells to MA. It is revealed that the use of a fully predictive active

formulation of SF contractility and remodelling is required to accurately capture the response of spread adhered cells over a range of applied pressures. Finally, experimental-computational quantification of nucleus deformability during MA of spread cells is presented.

2 Materials and Methods

2.1 Sample Preparation

Human umbilical vein endothelial cells (HUVEC) were obtained from Promocell (C-14010, Heidelberg, Germany) and grown as per Promocell protocols [23]. Cells are seeded onto gridded coverslips (Bellco, 1916-92525, NJ, USA) inside petri dishes. The alpha-numeric grid, photoetched onto the coverslips enables the relocation of specific cells. Cells are allowed to adhere to the substrate for two hours before 3 ml of media is added. The SF networks developed at this time result in a spread adhered cell morphology, consistent with previous studies [10]. In order to prepare cells in which the SFs have been disrupted, the media added at this point contains cytochalasin-D (cytoD) to inhibit actin polymerisation (Bio Sciences, Dublin, Ireland). CytoD concentrations (1 μM and 2 μM) and treatment times (≥30 minutes) used are based on previous studies [24, 25]. The protocol is verified by immuno-fluorescent staining and also by MA of cytoD treated cells (cytoD cells) with varying molarity concentrations. Experiments are performed on all cells 3±0.5 hours after reseeding.

2.2 Microscopy and Visualisation Technique

The prepared cells are loaded into a custom built MA system mounted on a live cell imaging microscope with environmental chamber (Olympus, IX-51 inverted microscope, Southend, UK). The environmental chamber enables incubation conditions (37°C and 5% CO_2) to be maintained during MA experiments. In order to monitor MA of cells on flat horizontal substrates using an inverted microscope, a mirror (Thorlabs Ltd., PFSQ10-03-P01, Cambridgeshire, UK) is positioned in contact with the substrate aligned at a 45° angle (Figure 1-D). The system facilitates visualisation of the target cell from multiple perspectives during experiments (bottom-up or from the side). The mirror configuration obstructs the microscopes' in-built light source, hence it is necessary to use a separate LED light source to illuminate the area beneath the mirror. It is important to note that incandescent light overheats cells, leading to necrosis. To utilise the optical path created by the mirror, the focal plane of the objective must be adjusted through the monolayer until the reflected image of the cells is observed (Figure 1-D). A long working distance objective is required in order to obtain usable focal planes.

2.3 Micropipette Aspiration Rig and Data Acquisition

Custom designed micropipette tips (TPC, Thebarton, Australia) are attached to a pressure control system and micromanipulator (Sutter Instruments, MM-1, CA, USA) using a modified microelectrode holder (A-M Systems, WA, USA). Micropipettes have a radius of 5 μm (R_{pip}) and

have a 50° bend 1 mm from the tip to facilitate positioning sufficiently close to the 45° aligned mirror. Micropipettes are coated with a siliconising reagent (Sigmacote, SL2, Sigma-Aldrich Ireland Ltd., Arklow) to inhibit cell adhesion. Using the micromanipulator and multiple perspective visualisation capability, the micropipette tip is positioned above the cell. The micropipette is then lowered until contact with the cell surface is established, leading to a light seal. The aspiration pressure is then applied instantaneously by turning a 3-way stopcock. Pressure is generated using a u-tube manometer and fluctuations are minimised using a damping chamber that is filled with phosphate buffered saline (PBS). This method of pressure control is similar to a previously described MA system [2].

The applied pressure is maintained for 300 s and the cell begins to deform into the micropipette gradually over time. Image sequences are acquired at 2 frames/s, from which the aspiration length, L_A, is measured using ImageJ software [26]. Aspiration length is the distance between the opening of the micropipette tip where the cell enters, and the furthermost point of the cell inside the micropipette (Figure 2-A(iv)). Aspiration lengths are normalised by the micropipette diameter (L_A/R_{pip}), and plot as a function of time, t (in seconds, s). Statistical analysis is performed using Minitab ver. 16 (Minitab Ltd., Coventry, UK). A two-way analysis of variance (ANOVA), with time and pressure as the independent factors, is used with a Tukey HSD test to examine the effect of the pressure variation on control cells. Student t-tests are used to test the significance of cytoD cell results. For all comparisons, statistical significance is declared if $p<0.05$.

2.4 Immuno-fluorescent Staining

After 300 s of MA, cells are fixed using a 4% paraformaldehyde solution. Fixed cells are treated with 0.1% triton solution for 5 mins to permeablise. Cells are then kept in a blocking solution of 10% FBS fetal bovine serum in PBS for 30-60 mins. Rhodamine conjugated phalloidin and Hoechst Dye 33342 (Molecular Probes, Life Technologies, NY, USA) are used to stain the actin filaments and nucleus, respectively. Washing 3 times with PBS is performed before and after each step. The coverslips containing cells are prepared for confocal imaging by mounting on glass slides. Prolong Gold Antifade Reagent (Molecular Probes, Life Technologies, NY, USA) is used to preserve staining quality and samples are kept below 4°C before obtaining fluorescent images. An Andor Revolution spinning disk confocal microscope (Yokogawa CSU-X1 Spinning disk unit & Olympus IX81 microscope) is used to image fluorescently stained samples. The cell of interest is found by returning to the recorded location on the coverslip's alpha-numeric grid using phase-contrast before z-stacks images of the aspirated cell are obtained. Two image channels are captured at each plane of focus, using laser excitation of 405 nm to visualise the nucleus and excitation of 564

nm to visualise the actin filaments. A step size of 1 µm is used between each z-plane. Z-stack images are processed using Andor IQ software version 2.3. 3D kymography based on the captured z-stacks is also performed using Andor iQ software.

2.5 Computational Methods

A bio-chemo-mechanical framework that considers the biochemistry inherent to SF formation, active contractility, and tension dependant dissociation is used to simulate the actin cytoskeleton in the cytoplasm [27]. Summarising the 3D active SF framework, which is described in full by Deshpande et al. [27] and Ronan et al. [20], a first order kinetic equation is used to capture formation and dissociation of SFs:

$$\frac{d\eta}{dt} = [1-\eta]\frac{Ck_f}{\theta} \; - \; \left[1-\frac{\sigma}{\sigma_0}\right]\eta\frac{k_b}{\theta} \tag{1}$$

where η is the non-dimensional activation level of a SF $(0 \leq \eta \leq 1)$. k_f and k_b are forward and backward reaction rate constants, respectively. C is an activation signal for SF formation that decays over time ($C = \exp(-t/\theta)$). θ is a decay constant for the signal.

To simulate the contractile behaviour of the fibre bundle a Hill-like equation is used:

$$\frac{\sigma}{\sigma_0} = 1 + \frac{\overline{k_v}}{\eta}\frac{\dot{\varepsilon}}{\dot{\varepsilon_0}}; \quad -\frac{\eta}{\overline{k_v}} \leq \frac{\dot{\varepsilon}}{\dot{\varepsilon_0}} \leq 0 \tag{2}$$

where $\dot{\varepsilon}$ is the fibre contraction/extension strain rate. This equation gives fibre tension normalised by the isometric tension level bound by zero and the model parameters, $\overline{k_v}$ and $\dot{\varepsilon}_0$. For fibres with a small negative strain, the tension will increase up to the isometric tension level ($\sigma_0 = \eta\sigma_{max}$) at zero strain rate. Fibres with a smaller negative strain rate ($\dot{\varepsilon}/\dot{\varepsilon_0} < -\eta/\overline{k_v}$) exhibit zero tension, and those undergoing positive strain rate ($\dot{\varepsilon} > 0$), have a constant tension equal to the isometric tension. The active framework is implemented in a *user-defined material subroutine* (*umat*) in the finite element software Abaqus 6.9 (Simula, Providence, RI, USA). In order to visualise areas of high SF alignment for direct comparison with fluorescent images, the variance parameter $(\Pi = \eta_{MAX} - \bar{\eta})$ is calculated at each integration point and used in Abaqus/CAE contour plots. $\bar{\eta}$ is the average activation level of all SFs at each point in the cytoplasm ($\bar{\eta} = \sum_{k=1}^{n}(\eta_k/n)$). To simulate experiments in which SFs have been eradicated, the active formulation is removed from the cytoplasm material make-up, leaving only passive elements in the cell.

A neo-Hookean hyperelastic formulation is used to model the passive non-contractile cytoplasm and nucleus behaviour in the cell. The neo-Hookean stress tensor is given as:

$$\sigma_{ij} = \frac{G}{J}\left(\bar{B}_{ij} - \frac{1}{3}\bar{B}_{kk}\delta_{ij}\right) + K(J-1) \tag{3}$$

where G and K are material shear and bulk moduli, respectively, and $\bar{B}$ is determined from the deformation gradient, F:

$$\bar{B}_{ij} = \frac{B_{ij}}{J^{2/3}} = \frac{F_{ik}F_{jk}}{(\det(F))^{2/3}} \tag{4}$$

Passive viscoelastic material behaviour is modelled using a one term Prony series:

$$G(t) = G\left(1 - \bar{g}^p\left(1 - e^{-t/\tau}\right)\right) \tag{5}$$

$$K(t) = K\left(1 - \bar{k}^p\left(1 - e^{-t/\tau}\right)\right) \tag{6}$$

where τ is the time constant for the material. $\bar{g}^p$ and $\bar{k}^p$ are dimensionless Prony series parameters used in the calculation of long-term shear ($G(t)$) and bulk ($K(t)$) moduli, respectively. The subscripts 'cyto' and 'nucl' are used to denote passive material properties associated with the cytoplasm and nucleus, respectively.

2.6 Finite Element Model Development

Cell base radius (R_C), nucleus radius (R_N), and cell height (H_C) are acquired from fluorescent and brightfield images using ImageJ software and are used to determine cell geometries (Figure 1). Cell and nucleus radii are calculated from a sample of measured areas (Figure 1-A). Height is measured directly from brightfield side view images (Figure 1-B). An axisymmetric mesh is generated based on geometrical measurements. An axisymmetric rigid body is used for the micropipette and micropipette-cell contact is assumed to be frictionless. It should be noted that for the axisymmetric cell geometry, the full 3D stress tensor is calculated as SFs are not confined to the axisymmetric plane. Further simulations were performed to ensure that the micropipette fillet radius has a minimal affect on computed aspiration length (data not shown). A rigidly bonded interaction between the cell and substrate is assumed.

Before MA is simulated in contractile cells, an equilibrium distribution of SFs is computed in the cell. This initial analysis step represents the seeding of untreated contractile cells on the substrate. This step is not required for cytoD cell simulations. In the next analysis step, the

micropipette is moved into a position so that it is just in contact with the cell membrane, and pressure is ramped up linearly over a 5 s period using a user-defined non-uniform distributed load subroutine. In order to mimic experimentally applied loading, pressure is applied to the cell membrane within the micropipette only. The constant pressure is maintained for a further 300 s while deformation occurs. The aspiration length is measured as the distance from the micropipette entrance to the furthermost point of the cell within the micropipette, similar to experimental methods.

3 Results

3.1 MA of Untreated and CytoD Treated Adhered Cells

In Figure 2-A, typical experimental images of cytoD treated and untreated cells are shown prior to the application of the aspiration pressure. A spread morphology is observed for untreated contractile cells (Figure 2-A(i)) with a highly developed network of SFs (Figure 1-A). Treatment with cytoD results in a break-down of all SFs in the cell, altering the morphology (as illustrated in the online supplementary material). Prior to aspiration, the measured height of cytoD cells is found to be 9.2±2.0 μm (Figure 2-A(iii)) compared to 6.8±1.6 μm for untreated cells. This demonstrates that the contractile action of the actin cytoskeleton reduces cell height.

Upon the application of a 100 Pa pressure, the cell aspirates approximately 5.3±1.9 μm into the micropipette after 300 s, as shown in Figure 2-A(ii). Application of a 100 Pa pressure to the cytoD treated cell results in a much higher aspiration length of 10.8±2.0 μm (Figure 2-A(iv)). This demonstrates that the removal of the actin cytoskeleton results in a more deformable cell.

Figure 2-B shows aspiration length as a function of time for untreated and cytoD cells. CytoD cell aspiration length is significantly higher than that of an untreated cell (p<0.05 at all time points); aspiration lengths for cytoD cells are ~2 times higher than untreated cells over the 300 second time span following pressure application. A similar curve shape is observed for both groups, with 70-75% of aspiration occurring within 100 s in all cases. Doubling the cytoD concentration from 1 μM to 2 μM has no statistically significant effect on cytoD aspiration length at any point (p>0.05).

As detailed in Section 2.5, cytoD cells are simulated using passive material models. A good fit is established with experimentally measured aspiration data for the cytoD treated cells, as shown in Figure 3-A. Hyperelastic material parameters are specified in Table 1. Prony series parameters are $\bar{g}_{cyto}^{P}$ = $\bar{k}_{cyto}^{P}$ = 0.9 and τ_{cyto} = 20 s. The contribution of SFs to the mechanical response of untreated cells is simulated via a computational framework that accounts for SF formation, remodelling, and contractility. It is demonstrated in Figure 3-A that the addition of the active framework (in parallel with the passive cytoplasm material behaviour calibrated for the cytoD cell) results in a significant reduction in aspiration length, in agreement with experimental data. Importantly, these active SF model parameters are used, without exception, for all active simulations presented in the current study. It should be stressed that the response of the active cell to MA is not achieved by simply calibrating a passive material model; rather, it is achieved by superimposing an active bio-chemo-mechanical framework for SF remodelling and contractility onto the passive material components (calibrated for a cytoD cell above). In essence, Figure 3-A

demonstrates the ability of the modelling framework to accurately represent the experimentally parsed contribution of the actin cytoskeleton to MA.

Table 1: Properties for material models used to represent the nucleus and cytoplasm.

	Passive Parameters		Active SF Model Parameters					
Cytoplasm	G_{cyto} (kPa)	K_{cyto} (kPa)	k_f	k_b	σ_{max} (kPa)	θ (s)	$\overline{k_v}$	$\dot{\varepsilon}_0$ (s^{-1})
	0.026	0.25	1	30	3	70	1	0.003
Nucleus	G_{nucl} (kPa)	K_{nucl} (kPa)						
	0.07	2.5						

In Figure 3-B, contour plots of the max principal stresses resulting from simulations are shown. Prior to the application of pressure, significant stresses are computed throughout the cytoplasm of the active cell due to SF contractility (Figure 3-B(iii)), whereas the passive cell is in a stress-free state (due to an absence of contractile SFs) (Figure 3-B(i)). In Figure 3-B(ii) and -B(iv), stress contours in the passive and active cells are shown after a 100 Pa pressure is applied for 60 s. Even though the passive cell is aspirated further into the micropipette, the observed cytoplasm stresses are smaller than in the active cell cytoplasm, showing that the active stresses generated by the SF framework dominate the stress state in the active cell even when applied deformations are large. It should also be noted that the deformed nucleus shape and nucleus stress distribution for the passive cell differs from that of the active cell.

3.2 MA of Untreated Spread Adhered Cells over a Range of Applied Pressures

Figure 4 shows the experimentally observed aspiration length as a function of time for a range of applied pressures (100 Pa, 500 Pa, and 800 Pa). All tests are performed on untreated contractile cells (it should be noted that full detachment of cytoD treated cells occurred for applied pressures of 500 Pa, whereas untreated cells remain fully adhered for all reported tests). As expected, higher applied pressures result in higher aspiration of the cell into the micropipette. Computational simulations using the active SF framework are also shown in Figure 4-A. The active model provides accurate predictions of cell aspiration length for the range of pressures considered experimentally. It is critical to note that active cell model parameters calibrated in Figure 3 are used for all simulations presented in Figure 4-A. In contrast to the active model, the passive viscoelastic model for the cytoplasm does not provide accurate predictions, as shown in Figure 4-B. This simplified viscoelastic model parameters are fitted to provide a reasonable prediction of the 100 Pa experimental data. However, highly inaccurate results are computed for simulation of the cell response to applied pressures 500 Pa and 800 Pa. This important result

clearly demonstrates the inadequacy of passive cell models which ignore the biomechanical behaviour of the actin cytoskeleton. Finally, unless otherwise stated, it should be noted that nucleus properties of $G_{nucl} =$ 0.07 kPa and $K_{nucl} =$ 2.5 kPa are used in all simulations. The mechanical behaviour of the nucleus is considered further in the following section (3.3).

In Figure 5-A(top), a typical brightfield microscopy image of an untreated contractile cell subject to 500 Pa pressure for 300 s is shown. Fluorescent imaging is performed to visualise the actin cytoskeleton and nucleus following MA. By the 3D rendering of z-stacks obtained using confocal microscopy, a side view of a deformed cell is acquired, as shown in Figure 5-A(bottom). It is clear from the side view profile that the nucleus is completely aspirated into the micropipette in the 500 Pa experiment, with SFs being confined to the outer radius of the aspirated section of the cell and the cell base. A computational simulation using the active modelling framework is presented in Figure 5-B, showing the predicted deformed cell morphology and SF distribution, again for a 500 Pa MA pressure applied for 300 s. Similar to the experimental image, the entire nucleus is predicted to aspirate into the micropipette. SFs are predicted to extend from the base of the cell into the micropipette. The aspirated SFs are computed near the outer surface of the cell, even in the region below the micropipette where there is no nucleus present (Figure 5-B(i)). Inside the micropipette the nucleus occupies the majority of the aspirated volume, with predicted SFs occurring to the sides (Figure 5-(ii)) and above (Figure 5-B(iii)) the nucleus.

Further fluorescent images are shown in Figure 6; selected z-stacks at four different levels are presented. The base slice in each case shows a significant distribution of SFs near the base of the cell. At the micropipette entrance, fibres are predominantly found at the outer radius of the aspirated portion of the cell. It should be noted that the arrangement of SF at this level is not due to the presence of the nucleus, as the fully aspirated nucleus is positioned above the micropipette entrance in all cases. The aspirated nuclei are surrounded by SFs, as evidenced by the mid aspiration and top of aspiration slices. Out of plane 3D rendered images of two of the aspirated cells are shown in Figure 7. Distinct bands of SFs extending vertically in the aspirated portion of the cell can be observed in Figure 7-A. Aligned SFs extending into the micropipette entrance are evident in Figure 7-B, with a high density of actin in the aspirated section. Kinking or bending of the aspirated portion can occur due to the fixing and staining protocol performed prior to fluorescent imaging. However, the overall SF distributions are visible from Figures 5-7 despite this unavoidable experimental drawback.

3.3 Investigation of Nucleus Mechanical Behaviour

In all simulations presented above, a nucleus shear modulus of 0.07 kPa and bulk modulus of 2.5 kPa are used. These values are determined from a detailed parametric investigation, as illustrated in Figure 8. Simulations are performed for an applied pressure of 500 Pa and corresponding experimental data are reproduced in all plots for comparison. In Figure 8-A a parametric investigation of nucleus shear modulus is presented (for a constant bulk modulus of 2.5 kPa). An excellent correlation with experimental results is obtained for a shear modulus 0.07 kPa. An increase in shear modulus from 0.07 to 0.1 kPa results in a 33% decrease in aspiration length at 300 s, demonstrating that computed aspiration length is highly sensitive to nucleus shear modulus. As is evident in Figure 8-A, a change in shear modulus also significantly affects the aspiration rate (slope of the curve), again only a value of 0.07 kPa provides an accurate prediction of experimental results.

In Figure 8-B a range of shear moduli is again considered, but for a lower bulk modulus of 0.2 kPa. In this case no value of shear modulus provides an accurate representation of the experimental aspiration curve. For a shear modulus of 0.1 kPa the correct aspiration length is computed at 300 s, but computed values are inaccurate at earlier time points due to an incorrect aspiration rate. It should be noted that, for both the high bulk modulus (Figure 8-A) and the low bulk modulus (Figure 8-B), the nucleus is computed to fully aspirate into the micropipette only if the shear modulus is less than 0.1 kPa. It should be recalled from the experimental images of Figures 5-7 that the nucleus fully aspirates into the micropipette for an applied pressure of 500 Pa.

In Figure 8-C a range of nucleus bulk moduli is considered while shear modulus is kept at a constant value of 0.14 kPa. In this case no bulk modulus value gives an accurate representation of the experimental aspiration curve. A substantial increase in bulk modulus from 1 kPa to 40 kPa results in only a 12% decrease in aspiration length at 300 s demonstrating that computed aspiration length is relatively insensitive to bulk modulus changes in this range. For a reduction of the bulk modulus to a value less than 1 kPa an increase in aspiration length is computed. However, the computed aspiration rate is not affected by the bulk modulus and is lower than the experimentally observed aspiration rate for a shear modulus of 0.14 kPa considered in Figure 8-C. It should also be noted that for this value of shear modulus, the lowest bulk modulus considered in Figure 8-C (0.093 kPa) corresponds to a Poisson's ratio of zero. Therefore, for the given shear modulus (0.14 kPa), full aspiration of the nucleus into the micropipette is not possible, regardless of the bulk modulus used.

In Figure 8-D a range of bulk moduli is again considered but for a lower shear modulus of 0.07 kPa. As noted above in Figure 8-A, this value of shear modulus in conjunction with a bulk modulus of 2.5 kPa provides a good agreement with the experimental data. However, as is evident in Figure 8-D, any value of bulk modulus in the range from 1 kPa to 40 kPa provides a reasonable prediction of the experimental behaviour. For bulk moduli less than 1 kPa computed aspiration lengths are higher than those observed experimentally. However, the computed aspiration rate is insensitive the value of bulk modulus, with all computational curves being parallel to the experimental curve in Figure 8-D. Importantly, full aspiration of the nucleus is computed for all simulations reported in Figure 8-D.

Finally, the deformed cell and nucleus morphology following an applied pressure of 500 Pa for 300 s is shown in Figure 9-A for the best fit nucleus properties, as determined in Figure 8 ($G_{nucl} =$ 0.07 kPa and $K_{nucl} = 2.5$ kPa). The fully aspirated nucleus is positioned above the entrance to the micropipette, as observed in experimental images (Figure 5-A(bottom) and Figure 6-(A-C)). The aspect ratio of the deformed nucleus is computed as 1.6, which is within the standard deviation of the experimentally measured value (1.5±0.20) (Figure 9-E). As shown in Figure 9-B, when the bulk modulus is reduced to 0.2 kPa both the computed aspiration length (as shown in Figure 8-B) and nucleus aspect ratio exceed the values observed experimentally. As shown in Figure 9-C and -D the value of shear modulus is excessively high, preventing full aspiration of the nucleus into the micropipette. In addition to predicting incorrect aspiration curves (as shown in Figure 8-C), incorrect nucleus aspect ratios are also computed (Figure 9-E). In relation to the most accurate prediction of nucleus aspect ratio (Figure 9-A), it should be noted that extremely high values of maximum principal strain (~130%) are computed in the nucleus, demonstrating that the cell nucleus is highly deformable. As expected, an inaccurate prediction of cell aspiration length results in an inaccurate prediction of nucleus strain.

4 Discussion

The current study presents a investigation of the role of the actin cytoskeleton in the micropipette aspiration (MA) of spread adhered cells. The following key contributions are highlighted: (i) a custom system is developed to allow visualisation of the MA of adhered cells, uncovering the contribution of the actin cytoskeleton to cell aspiration; (ii) it is demonstrated that an active computational framework that incorporates SF remodelling and contractility must be used in order to accurately simulate the MA of untreated cells; and (iii) experimental imaging reveals that the cell nucleus is fully aspirated into the micropipette at higher applied pressures, with corresponding computational simulations demonstrating that the nucleus is highly deformable, undergoing high levels of strain (>100%). These key findings present a significant advance on previous MA studies and to the general understanding of the role of the actin cytoskeleton and nucleus to cell biomechanical behaviour.

A custom MA system for the biomechanical investigation of cells adhered to a substrate is used in the current study. Due to the complexity of visualising MA of substrate adhered cells, previous MA studies have focused primarily on cells suspended in media. In particular, suspended endothelial cells [2-4], suspended chondrocytes [5-7], suspended stem cells [8], and suspended fibroblasts [9] have been tested using the MA technique. However such studies are of limited value as these cell phenotypes are typically not found suspended *in vivo*; rather, they adhere to an extra cellular matrix. Moreover, the cytoskeletal structure and biomechanical behaviour of such cells is markedly different when adhered to a substrate, in comparison to the suspended state [2, 10]. Therefore, the development of an MA system for the investigation of the biomechanical behaviour of cells when adhered to a substrate is of significant value. In an effort to study the mechanical behaviour of spread adhered endothelial cells, Byfield et al. [28] oriented a micropipette parallel to the substrate, leading to highly localised measurements at the outer edge of the cell-substrate contact region. In order to achieve non-localised measurements representative of whole cell behaviour, a precisely-positioned large diameter micropipette aligned perpendicular to the substrate should be used. In the study of Thoumine et al. [16] the substrate was rotated by 90° to facilitate visualisation of the aspirated cell. However, using this approach the micropipette can be viewed only from the side, hence precise three-dimensional positioning of the micropipette over the centre of the cell is not possible. Furthermore, relocation of aspirated cells post-aspiration for a confocal microscopy investigation of the stained deformed actin cytoskeleton is not possible using this approach. In the current study, a custom designed system that allows for both side and bottom-up views of cells and the micropipette is developed.

This facilitates: (i) the precise three-dimensional positioning of the micropipette over the centre of the cell using multiple perspectives; and (ii) the visualisation of the aspirated section of adhered cells using a micropipette aligned perpendicular to the substrate. The system also enables further examination of the actin cytoskeleton of aspirated cells using confocal microscopy.

It is demonstrated in the current study that untreated contractile spread adhered cells undergo significantly less aspiration into the micropipette than cells in which the actin cytoskeleton has been chemically inhibited (cytoD cells); therefore, the actin cytoskeleton increases the resistance of cells to MA. Fluorescent staining demonstrates that SFs are stretched into the micropipette during MA. Clearly the tension exerted by aspirated stretched SFs contributes significantly to the mechanical response of the cell. The current study demonstrates that MA provides a robust and controlled experimental method of applying a tensile load to *in cyto* actively contractile SFs. Previous efforts to characterise the tensile behaviour of SFs have relied on isolation/extraction of individual SFs from the cell, followed by tensile testing [29]. It is important to note that isolated/extracted SFs behave as a passive material [30], neglecting the critically important features of active myosin induced cross-bridge cycling and remodelling. The applicability of the active SF formulation used in the current study has been validated for a range of cell phenotypes and loading regimes [19, 20]. A recent study of single chondrocytes by Dowling et al. [18] has demonstrated that localised stretching of SFs in tensile regions of the cytoplasm during applied shear significantly influences cell resistance to deformation, with dissociation of the actin cytoskeleton being observed in compressive regions of the cell. Additionally, the studies of Ronan et al. [20] and Weafer et al. [21] demonstrate that during parallel plate compression SFs in particular orientations are stretched, again increasing the resistance of cells to deformation. However, unlike applied shear and parallel plate experiments, the MA technique utilised in the current study allows for the application of precise tensile loads and accurate monitoring of SF strain rates in the aspirated section. In summary, the experimental observation of SF deformation under a controlled loading regime provides new insight into the mechanism by which the actin cytoskeleton contributes to the deformation resistance of spread cells. This may inform tissue engineering strategies [31, 32] and may have important implications for new pathologies [12, 33]. A link between actively generated cell tension and collagen production in a micro-tissue construct has recently been reported [34]. The experimental-computational approach presented in the current paper provides an advanced understanding of the relationship between externally applied force, SF active contractility, and nucleus deformation. Such a fundamental understanding at a single cell level is critical for the development of next-generation strategies for the precise

engineering of tissue constructs. A recent study highlights the ability of the active SF modelling framework to guide the *in vitro* engineering of cardiac tissue [35].

Previous studies have used simplified passive models analytical [3-5, 28] or numerical models of passive homogeneous elastic or viscoelastic cells to interpret experimentally observed aspiration curves. Typically such studies report elastic or viscoelastic material parameters based on a curve fit of experimental results. While it could be argued that a viscoelastic model may have some validity for the simulation of a un-adhered suspended cell, which do not contain a network of SFs, the current study clearly demonstrates such a simplistic modelling approach is not appropriate for spread adhered cells. Specifically, it is demonstrated that such a passive material model does not capture the experimentally observed response if the applied pressure is changed. Hence the curve-fitting of viscoelastic material properties to a MA curve is entirely dependent on the applied pressure used experimentally. In addition to the inability of a passive viscoelastic cell model to predict cell aspiration over a range of applied pressures, an earlier study by Thoumine et al. [16] demonstrates that elastic stiffness and viscosity must be significantly altered as a function of the level of cell spreading. Furthermore, a study by McGarry and McHugh [15] demonstrates that when the cytoplasm is modelled as a passive viscoelastic, the cell elastic stiffness must be artificially increased as a function of spreading in order to capture *in vitro* cell detachment forces.

In the current study an active SF framework is used to investigate the biomechanical role of the actin cytoskeleton during the MA of spread adhered cells. It is demonstrated that the simulation of SF remodelling and contractility throughout the cytoplasm is critical in order to accurately predict experimentally observed cell response to a wide range (100 Pa - 800 Pa) of applied pressures. Furthermore, the predicted distribution of SFs is closely aligned with results of fluorescent images, i.e. SFs stretch along the long axis of the aspirated section of the cell forming a peripheral ring at the inner wall of the micropipette. The stretching of aligned contractile SFs along the axis of the micropipette provides an increased resistance to MA. When SFs are eliminated using the cytoD treatment the reduced resistance to deformation results in significantly increased aspiration length for applied pressures of 100 Pa, and aspiration of the entire cell into the micropipette at higher pressures ($\geq$500 Pa). It has been widely established in previous experimental studies that the actin cytoskeleton remodels during cell spreading, with spread cells exhibiting a highly developed network of contractile SFs [10, 11, 13]. The development of a network of contractile SFs underlies the vast differences in “apparent stiffness” between round and spread cells [16]. Furthermore, highly contractile cell phenotypes exhibit a higher apparent stiffness when subjected to cell compression. For example, very high

compression forces (~2500 nN) have been reported for spread myoblasts [36] whereas lower compression forces (~360 nN) have been reported for less contractile fibroblasts [37]. A recent study by Ronan et al. [20] demonstrates that the active SF model used in the in the current study is capable of capturing the relationship between the level of cell contractility and the compression resistance of spread cells. The current study advances on this work, providing a detailed experimental-computational quantitative analysis of the role of SF elongation during cell MA.

The current study provides a detailed investigation of nucleus deformation in single spread adhered cells subjected to MA. In the absence of external loading the coupled interaction between the actin cytoskeleton and the cell nucleus has recently been investigated experimentally [21, 38], where it is shown that the contractile action of apical SFs result in changes in nucleus morphology. Building upon this work, the MA technique presented in the current study allows for the precise application of force to this key region of the cell, and measurement of the resultant nucleus deformation and stress fibre extension/remodelling. This provides new data for validation and calibration of constitutive models for the nucleus and surrounding SFs, as presented in the current paper. A high level of nucleus deformation is observed; nuclei are fully aspirated into the micropipette for pressures of 500 Pa or higher, with nucleus strains in excess of 100% being computed. Simulations suggest that complete aspiration of the nucleus into the micropipette occurs only for very low nucleus shear modulus values (G_{nucl}<0.1 kPa). Simulating isolated nuclei, Vaziri et al. [39] also computes a low shear modulus based on experimental data for isolated endothelial cell nuclei [40] and isolated chondrocyte nuclei [7]. However, it should be noted that nucleus mechanical behaviour may be altered by the isolation technique used. It is demonstrated by Guilak et al. [7] that the long term mechanical properties of nuclei isolated using chemical and mechanical techniques are significantly different. Previous experimental studies of MA of suspended cells also reveal significant nucleus deformation [8, 41]. Furthermore, Pajerowski et al. [41] report that permanent viscoplastic deformation of the nucleus occurs due lamin A/C and chromatin remodelling. A careful characterisation of nucleus deformation, as presented in the current study for spread adhered cells, and in the study of Pajerowski et al. for suspended cells, is of critical importance as nucleus deformation has been linked to cell mechanotransduction due to the reshaping of nuclear lamina and alterations in chromatin distribution [42]. Direct modulation of nuclear shape has been shown to affect the regulation of type II collagen as well as gene expression [33]. Significant deformation of the nucleus has been observed *in situ* [43], and may have significant implications for *in vivo* mechanotransduction and cell migration. A high level of deviatoric deformation of the

nucleus during MA is computed in the current study. Anderson and Knothe Tate [44] report that such a stress state will result in stem cells differentiation towards an endothelial lineage. The characterisation of nucleus behaviour presented in the current study may aid the development and calibration of microfluidic devices for cell sorting [45] and direct cytosolic delivery of transcription factors [46].

The current study presents a number of significant advances in the field of experimental and computational single cell biomechanics, providing a platform for several further investigations. Future experiments in which the level of cell spreading is controlled via micro-patterned substrates should be performed to further investigate the relationship between cell geometry and the development of a highly contractile actin cytoskeleton [47, 48]. Furthermore, the role of substrate stiffness and adhesion promoting proteins [49, 50] in the biomechanical response of spread adhered cells to MA should be considered. The current technique only allows observation of SFs at the end of aspiration experiments. In order to observe the evolution of the actin cytoskeleton and nucleus deformation during experiments, fluorescent staining could be performed at a number of time points or live imaging techniques could be implemented, for example using F-actin transfection. Live imaging could also allow measurement of intracellular strain in experiments by tracking specific markers such as mitochondria in the cytoplasm [51] or DNA in the nucleus [43]. A recent study by Dowling et al. [18] demonstrates that the mechanical response of cells to applied shear is primarily influenced by the actin cytoskeleton, while the disruption of microtubules and intermediate filaments had a less significant effect on chondrocyte response. A future MA study in which microtubules and intermediate filaments are systematically disrupted would allow for the investigation of the role of these cytoskeletal components in the regulation of nucleus deformation. MA induced membrane and nucleus stretch could be used to examine the enhanced intracellular delivery of macromolecules such as carbon nanotubes, proteins and siRNA [46].

5 Conclusions

A custom system that facilitates the visualisation of adhered cells during MA is developed to experimentally investigate the contribution of the actin cytoskeleton to the spread cell biomechanical response. Additionally, computational simulations are performed in order to interpret experimentally observed phenomena. The current experimental-computational investigation uncovers a number of significant findings: (i) The significant contribution of the actin cytoskeleton to cell biomechanical behaviour during MA is demonstrated experimentally; (ii) a passive viscoelastic material model is not capable of capturing experimentally measured aspiration lengths over a range of applied pressures; (iii) an active SF model, including the key features of remodelling and contractility of the actin cytoskeleton, accurately predicts the response the cells over a range of applied pressures and the redistribution and stretching of SFs into the aspirated portion of the cell; and (iv) finally, a detailed experimental-computational investigation of the nucleus mechanical behaviour demonstrates that the nucleus is highly deformable *in cyto*, reaching strain levels in excess of 100% during MA. These findings represent a significant advancement in the understanding of the characterisation of the biomechanical behaviour of the actin cytoskeleton and cell nucleus.

6 Acknowledgments

Funding for this research was provided by Science Foundation Ireland – Research Frontiers Programme (10/RFP/ENM2960). The authors acknowledge Dr. L. M. McNamara for providing access to an Olympus IX-51 Inverted Microscope. The authors acknowledge Dr. Vikram Deshpande, Dr. Matthew Haugh and Dr. Muriel Voisin for helpful discussion.

7 References

1. Hochmuth RM. Micropipette aspiration of living cells. J Biomech 2000;33:15-22.
2. Sato M, Levesque MJ, Nerem RM. Micropipette aspiration of cultured bovine aortic endothelial cells exposed to shear stress. Arteriosclerosis 1987;7:276-86.
3. Sato M, Theret DP, Wheeler LT, Ohshima N, Nerem RM. Application of the micropipette technique to the measurement of cultured porcine aortic endothelial cell viscoelastic properties. J Biomech Eng 1990;112:263-8.
4. Sato M, Ohshima N, Nerem RM. Viscoelastic properties of cultured porcine aortic endothelial cells exposed to shear stress. J Biomech 1996;29:461-7.
5. Jones WR, Ping Ting-Beall H, Lee GM, Kelley SS, Hochmuth RM, Guilak F. Alterations in the Young's modulus and volumetric properties of chondrocytes isolated from normal and osteoarthritic human cartilage. J Biomech 1999;32:119-27.
6. Pravincumar P, Bader DL, Knight MM. Viscoelastic cell mechanics and actin remodelling are dependent on the rate of applied pressure. PLoS ONE 2012;7:e43938.
7. Guilak F, Tedrow JR, Burgkart R. Viscoelastic properties of the cell nucleus. Biochem Biophys Res Commun 2000;269:781-6.
8. Ribeiro AJ, Tottey S, Taylor RW, Bise R, Kanade T, Badylak SF, et al. Mechanical characterization of adult stem cells from bone marrow and perivascular niches. J Biomech 2012;45:1280-7.
9. Zhou E, Quek S, Lim C. Power-law rheology analysis of cells undergoing micropipette aspiration. Biomech Model Mechanobiol 2010;9:563-72.
10. Reinhart-King CA, Dembo M, Hammer DA. The dynamics and mechanics of endothelial cell spreading. Biophys J 2005;89:676-89.
11. Lemmon CA, Sniadecki NJ, Ruiz SA, Tan JL, Romer LH, Chen CS. Shear force at the cell-matrix interface: enhanced analysis for microfabricated post array detectors. Mech Chem Biosyst 2005;2:1-16.
12. Roy S, Thacher T, Silacci P, Stergiopulos N. Arterial biomechanics after destruction of cytoskeleton by cytochalasin D. J Biomech 2009;42:2562-8.
13. Barreto S, Clausen CH, Perrault CM, Fletcher DA, Lacroix D. A multi-structural single cell model of force-induced interactions of cytoskeletal components. Biomaterials 2013;34:6119-26.
14. Nawaz S, Sánchez P, Bodensiek K, Li S, Simons M, Schaap IAT. Cell visco-elasticity measured with AFM and optical trapping at sub-micrometer deformations. PLoS ONE 2012;7:e45297.
15. McGarry JP, McHugh PE. Modelling of in vitro chondrocyte detachment. J Mech Phys Solids 2008;56:1554-65.
16. Thoumine O, Cardoso O, Meister J-J. Changes in the mechanical properties of fibroblasts during spreading: a micromanipulation study. Eur Biophys J 1999;28:222-34.
17. Ofek G, Dowling EP, Raphael RM, McGarry JP, Athanasiou KA. Biomechanics of single chondrocytes under direct shear. Biomech Model Mechanobiol 2010;9:153-62.
18. Dowling EP, Ronan W, Ofek G, Deshpande VS, McMeeking RM, Athanasiou KA, et al. The effect of remodelling and contractility of the actin cytoskeleton on the shear resistance of single cells: a computational and experimental investigation. J R Soc Interface 2012;9:3469-79.
19. McGarry JP, Fu J, Yang MT, Chen CS, McMeeking RM, Evans AG, et al. Simulation of the contractile response of cells on an array of micro-posts. Philos Trans A Math Phys Eng Sci 2009;367:3477-97.
20. Ronan W, Deshpande VS, McMeeking RM, McGarry JP. Numerical investigation of the active role of the actin cytoskeleton in the compression resistance of cells. J Mech Behav Biomed Mater 2012;14:143-57.
21. Weafer PP, Ronan W, Jarvis SP, McGarry JP. Experimental and computational investigation of the role of stress fiber contractility in the resistance of osteoblasts to compression. Bull Math Biol 2013;75:1284-303.

22. Ronan W, Deshpande VS, McMeeking RM, McGarry JP. Cellular contractility and substrate elasticity: a numerical investigation of the actin cytoskeleton and cell adhesion. Biomech Model Mechanobiol 2013:http://dx.doi.org/10.1007/s10237-013-0506-z (In Press).
23. Promocell. Endothelial cells (large vessels) - Instruction manual. Heidelberg. Online. 2013 November. Available from URL: http://www.promocell.com/
24. Hayakawa K, Tatsumi H, Sokabe M. Actin stress fibers transmit and focus force to activate mechanosensitive channels. J Cell Sci 2008;121:496-503.
25. Nishitani WS, Saif TA, Wang Y. Calcium signaling in live cells on elastic gels under mechanical vibration at subcellular levels. PLoS ONE 2011;6:e26181.
26. Schneider CA, Rasband WS, Eliceiri KW. NIH image to ImageJ: 25 years of image analysis. Nat Methods 2012;9:671-5.
27. Deshpande VS, McMeeking RM, Evans AG. A model for the contractility of the cytoskeleton including the effects of stress-fibre formation and dissociation. Proc Math Phys Eng Sci 2007;463:787-815.
28. Byfield FJ, Aranda-Espinoza H, Romanenko VG, Rothblat GH, Levitan I. Cholesterol depletion increases membrane stiffness of aortic endothelial cells. Biophys J 2004;87:3336-43.
29. Katoh K, Kano Y, Masuda M, Onishi H, Fujiwara K. Isolation and contraction of the stress fiber. Mol Biol Cell 1998;9:1919-38.
30. Deguchi S, Ohashi T, Sato M. Tensile properties of single stress fibers isolated from cultured vascular smooth muscle cells. J Biomech 2006;39:2603-10.
31. Shen G, Tsung HC, Wu CF, Liu XY, Wang XY, Liu W, et al. Tissue engineering of blood vessels with endothelial cells differentiated from mouse embryonic stem cells. Cell Res 2003;13:335-41.
32. Shieh AC, Athanasiou KA. Principles of cell mechanics for cartilage tissue engineering. Ann Biomed Eng 2003;31:1-11.
33. Campbell JJ, Blain EJ, Chowdhury TT, Knight MM. Loading alters actin dynamics and up-regulates cofilin gene expression in chondrocytes. Biochem Biophys Res Commun 2007;361:329-34.
34. Kural MH, Billiar KL. Mechanoregulation of valvular interstitial cell phenotype in the third dimension. Biomaterials 2014;35:1128-37.
35. Thavandiran N, Dubois N, Mikryukov A, Massé S, Beca B, Simmons CA, et al. Design and formulation of functional pluripotent stem cell-derived cardiac microtissues. Proc Natl Acad Sci USA 2013;110:4698-707.
36. Peeters EA, Oomens CW, Bouten CV, Bader DL, Baaijens FP. Viscoelastic properties of single attached cells under compression. J Biomech Eng 2005;127:237-43.
37. Lulevich V, Zink T, Chen HY, Liu FT, Liu GY. Cell mechanics using atomic force microscopy-based single-cell compression. Langmuir 2006;22:8151-5.
38. Li Q, Kumar A, Makhija E, Shivashankar GV. The regulation of dynamic mechanical coupling between actin cytoskeleton and nucleus by matrix geometry. Biomaterials 2014;35:961-9.
39. Vaziri A, Mofrad MRK. Mechanics and deformation of the nucleus in micropipette aspiration experiment. J Biomech 2007;40:2053-62.
40. Deguchi S, Maeda K, Ohashi T, Sato M. Flow-induced hardening of endothelial nucleus as an intracellular stress-bearing organelle. J Biomech 2005;38:1751-9.
41. Pajerowski JD, Dahl KN, Zhong FL, Sammak PJ, Discher DE. Physical plasticity of the nucleus in stem cell differentiation. Proc Natl Acad Sci USA 2007;104:15619-24.
42. Dahl KN, Ribeiro AJ, Lammerding J. Nuclear shape, mechanics, and mechanotransduction. Circ Res 2008;102:1307-18.
43. Henderson JT, Shannon G, Veress AI, Neu CP. Direct measurement of intranuclear strain distributions and RNA synthesis in single cells embedded within native tissue. Biophys J 2013;105:2252-61.
44. Anderson EJ, Knothe Tate ML. Design of tissue engineering scaffolds as delivery devices for mechanical and mechanically modulated signals. Tissue Eng 2007;13:2525-38.

45. Yamada M, Kano K, Tsuda Y, Kobayashi J, Yamato M, Seki M, et al. Microfluidic devices for size-dependent separation of liver cells. Biomed Microdevices 2007;9:637-45.
46. Sharei A, Zoldan J, Adamo A, Sim WY, Cho N, Jackson E, et al. A vector-free microfluidic platform for intracellular delivery. Proc Natl Acad Sci USA 2013;110:2082-7.
47. Théry M, Pépin A, Dressaire E, Chen Y, Bornens M. Cell distribution of stress fibres in response to the geometry of the adhesive environment. Cell Motil Cytoskeleton 2006;63:341-55.
48. Chen CS, Mrksich M, Huang S, Whitesides GM, Ingber DE. Micropatterned surfaces for control of cell shape, position, and function. Biotechnol Prog 1998;14:356-63.
49. Byfield FJ, Reen RK, Shentu TP, Levitan I, Gooch KJ. Endothelial actin and cell stiffness is modulated by substrate stiffness in 2D and 3D. J Biomech 2009;42:1114-9.
50. Solon J, Levental I, Sengupta K, Georges PC, Janmey PA. Fibroblast adaptation and stiffness matching to soft elastic substrates. Biophys J 2007;93:4453-61.
51. Knight MM, Bomzon Z, Kimmel E, Sharma AM, Lee DA, Bader DL. Chondrocyte deformation induces mitochondrial distortion and heterogeneous intracellular strain fields. Biomech Model Mechanobiol 2006;5:180-91.

Appendix A

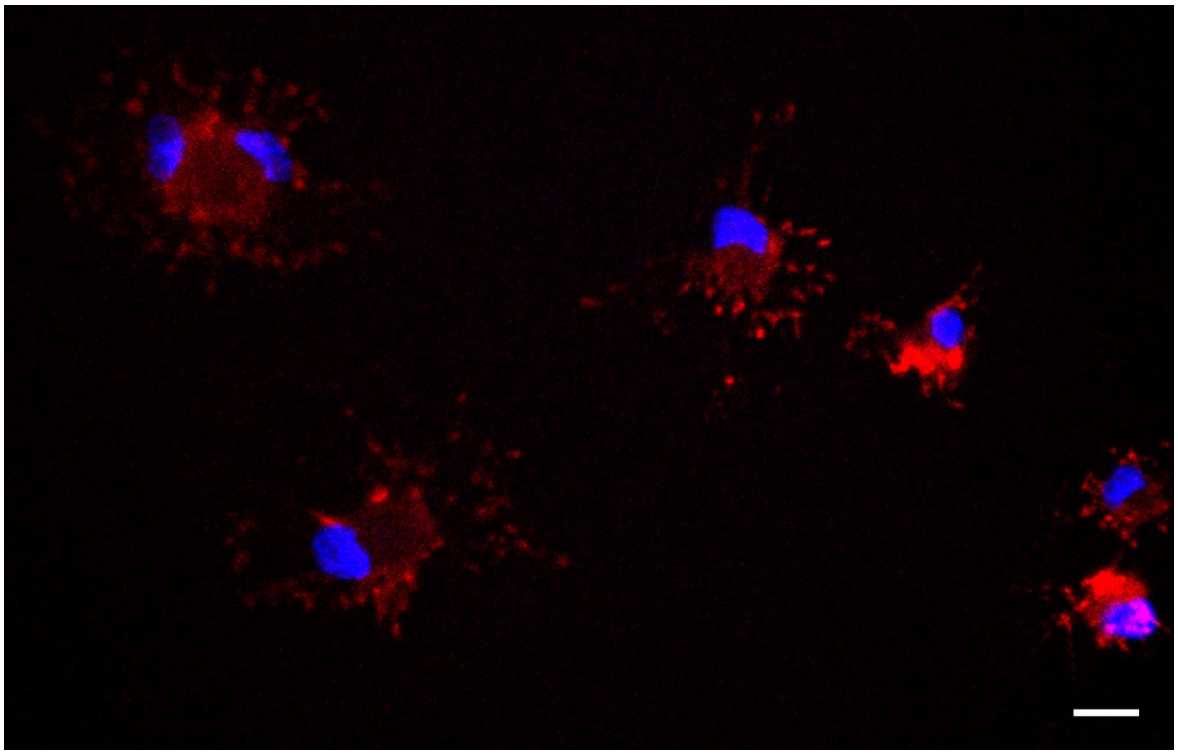

Figure A1: Representative fluorescent image of cytochalasin-D treated cells (cytoD cells) with actin shown in red and nuclei shown in blue. Scale bar = 20 µm.

Figures

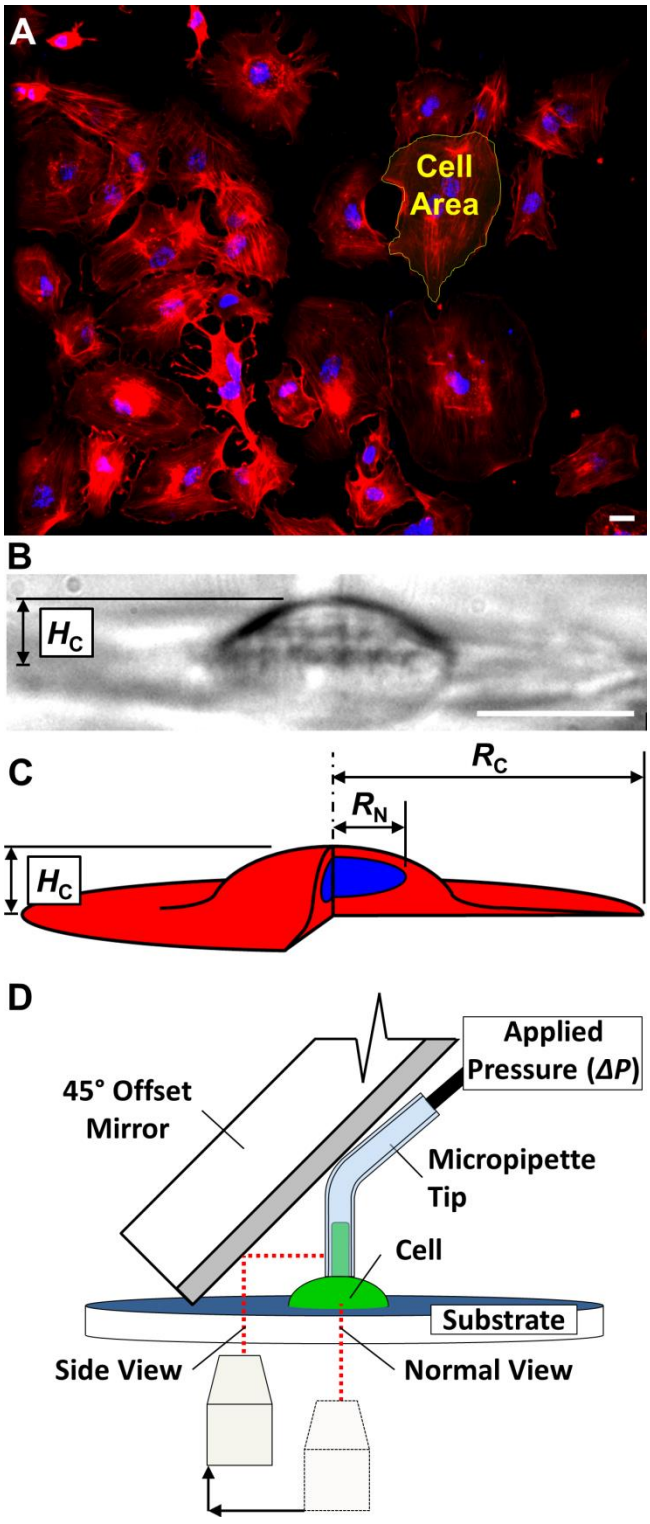

Figure 1: To generate cell geometries fluorescent and brightfield images of cells are utilised. (A) By measuring the area of cells and nuclei in fluorescent images, cell base radius (R_C) and nucleus radius (R_N) can be calculated. (B) Cell height (H_C) is measured directly from brightfield images. (C) Diagram of an idealised axisymmetric cell geometry indicating cell height and base radius. (D) MA is visualised using a mirror aligned at 45° to the substrate surface. Scale bars = 20 μm.

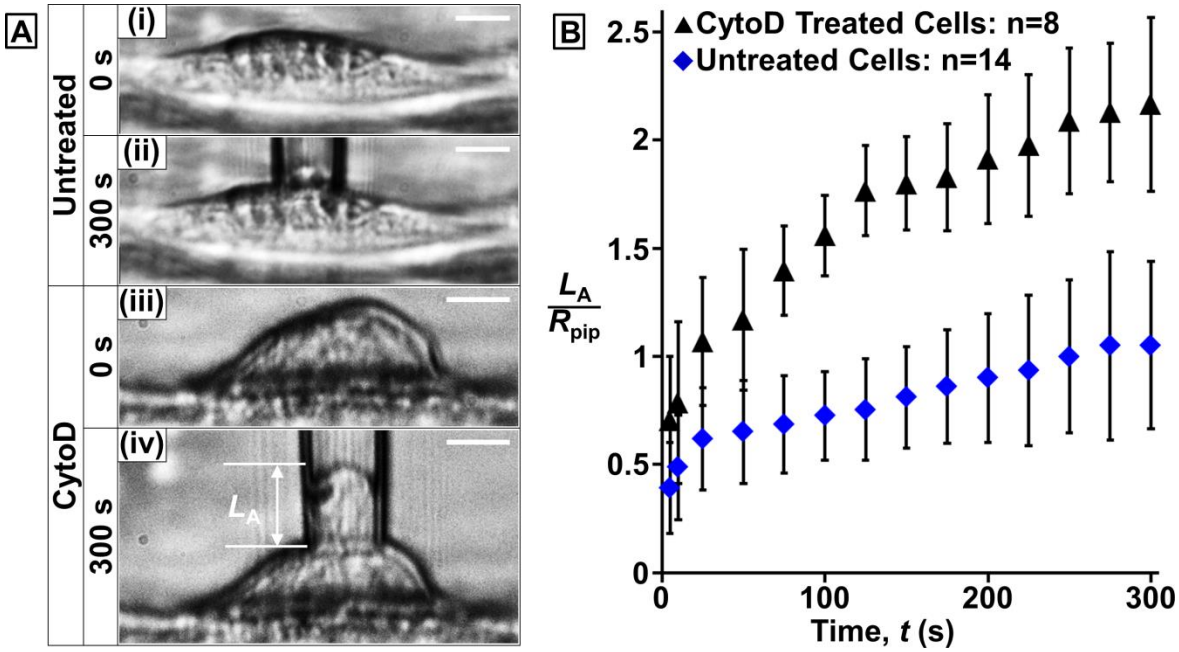

Figure 2: (A) Representative brightfield side view images of an an adhered untreated contractile cell and a cytoD treated cell are shown. (i) An untreated cell in a sub-confluent monolayer. (ii) Deformation of an untreated cell 300 s after pressure application. (iii) A cytoD treated cell in a sub-confluent monolayer. (iv) Deformation of a cytoD treated cell 300 s after pressure application. (B) Normalised aspiration length is shown as a function of time for cytoD treated and untreated cells. Note that all images and results correspond to a 100 Pa applied pressure. Scale bar = 10 μm.

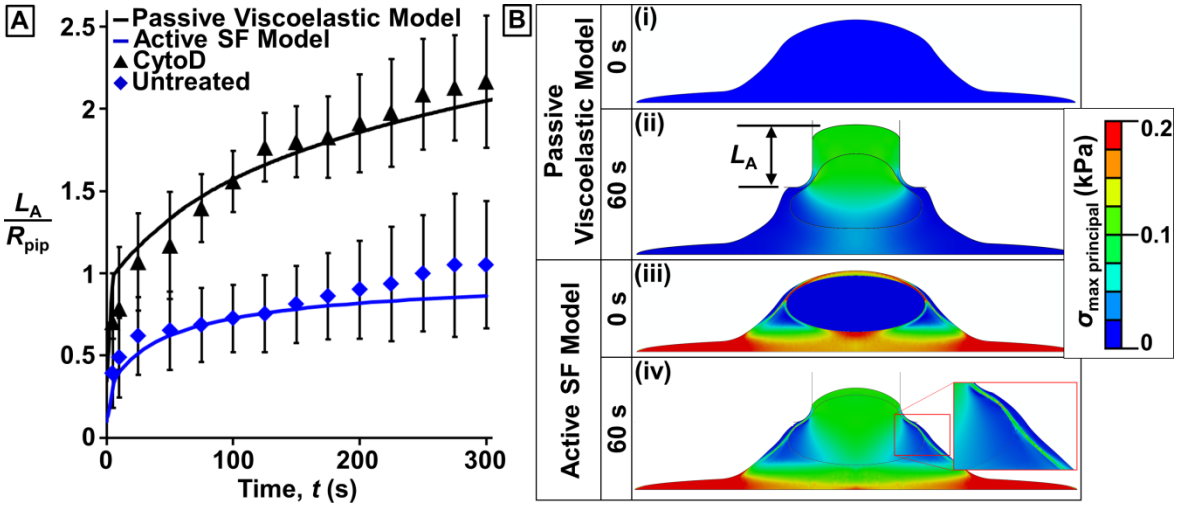

Figure 3: (A) Normalised computational and experimental aspiration length as a function of time for untreated and cytoD treated cells subjected to an applied pressure of 100 Pa. (B) Computed distribution of maximum principal stress ($\sigma_{\text{max principal}}$) in passive and active cell simulations. The passive viscoelastic model is used to simulate cytoD cell response and the active SF model is placed in parallel with the passive viscoelastic model to simulate untreated cell response. (i) Passive model prior to application of applied pressure (stress free reference configuration). (ii) Computed stress state in passive viscoelastic cell 60 s after pressure application. (iii) Stress state in the cell and nucleus prior to application of applied pressure, computed using the active SF model. (iv) Stress state in the cell and nucleus 60 s after pressure application, computed using the active SF model. Insert shows a zoomed image of the stress distribution at the entrance to the micropipette.

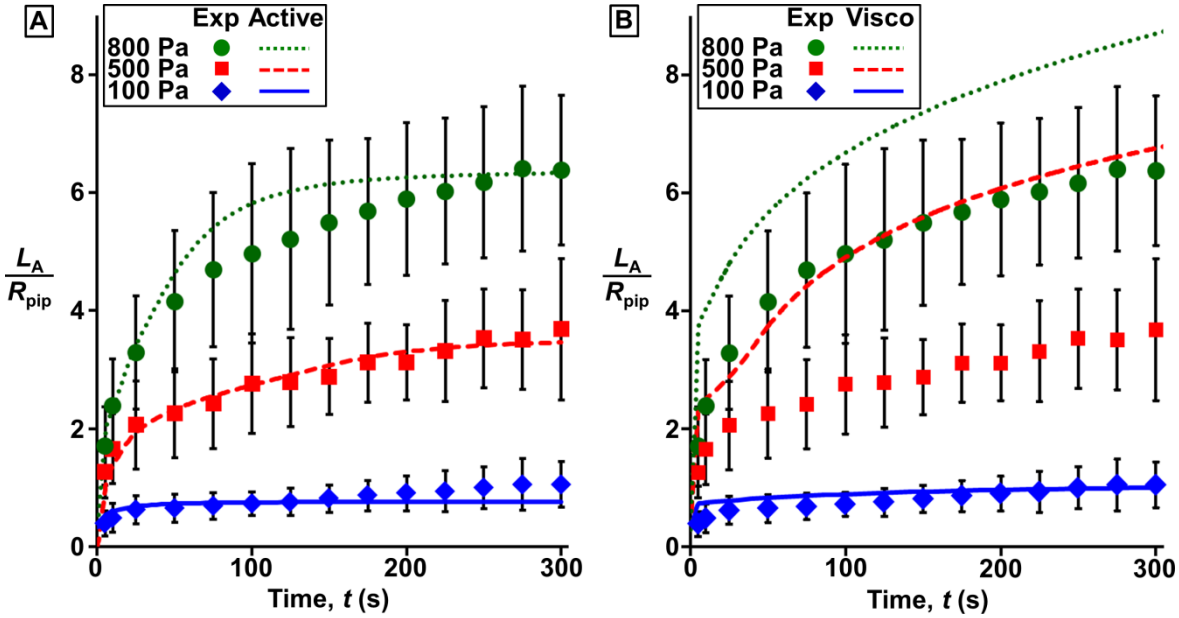

Figure 4: Normalised aspiration length as a function of time for untreated cells subjected to a range of applied pressures (100 Pa, 500 Pa, and 800 Pa). Symbols and error bars represent experimental (Exp) results (n≥10) and lines represent computational predictions. (A) Computed results using the active SF model (Active). (B) Computed results using a passive viscoelastic model (Visco) (G_{cyto} = 0.068 kPa, K_{cyto} = 0.67 kPa, $\bar{g}^P_{cyto} = \bar{k}^P_{cyto}$ = 0.9, τ_{cyto} = 40 s). Experimental results are superimposed in both (A) and (B) for direct comparison with computational predictions.

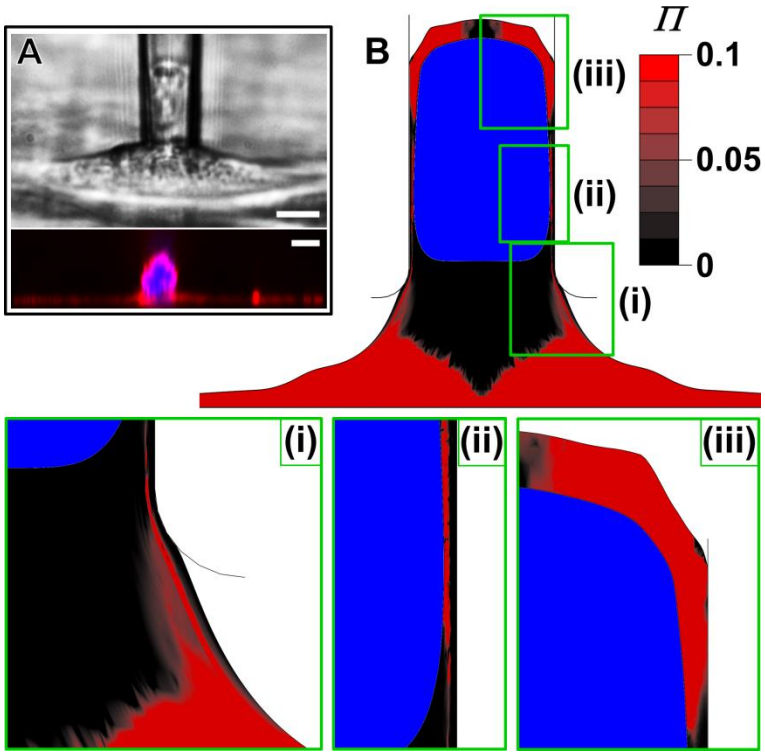

Figure 5: (A) Experimental brightfield (top) and 3D rendered fluorescent (bottom) side view images of aspirated cells. (B) Computed SF distribution (*Π*) in an aspirated cell using the active SF model. Zoomed-in images are shown at: (i) the micropipette entrance; (ii) mid-point of aspirated section; and (iii) top of the aspirated section of the cell. Results shown correspond to a pressure of 500 Pa applied for 300 s. Scale bars = 10 μm.

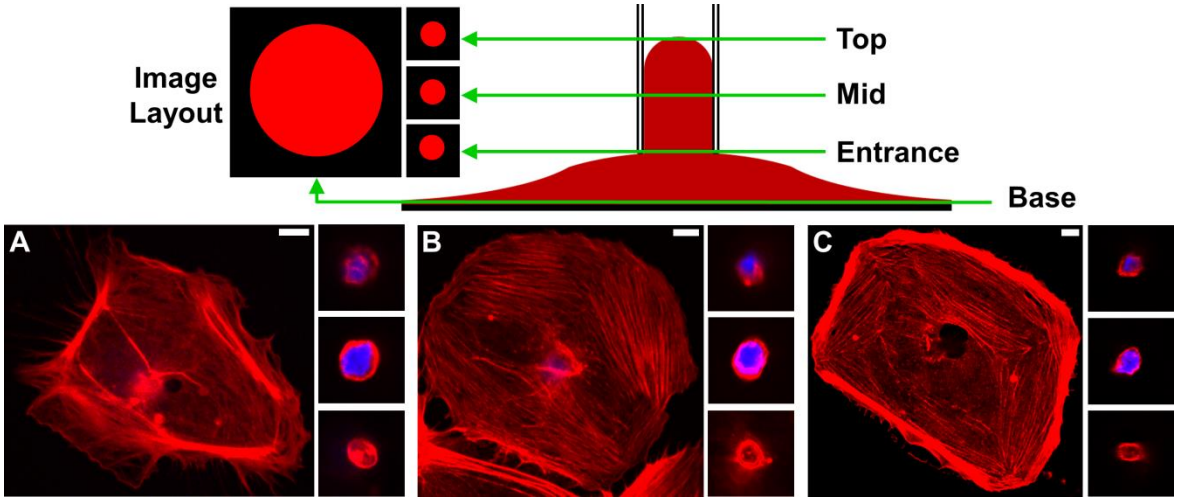

Figure 6: Individual z-stack images of aspirated cells fluorescently stained for SFs and nuclei for three cells (A-C). Stacks at the base of the cell (Base), at the micropipette entrance (Entrance), midway along the aspirated section of cell (Mid), and at the top of aspirated section of the cell (Top) are presented. Scale bars = 10 μm.

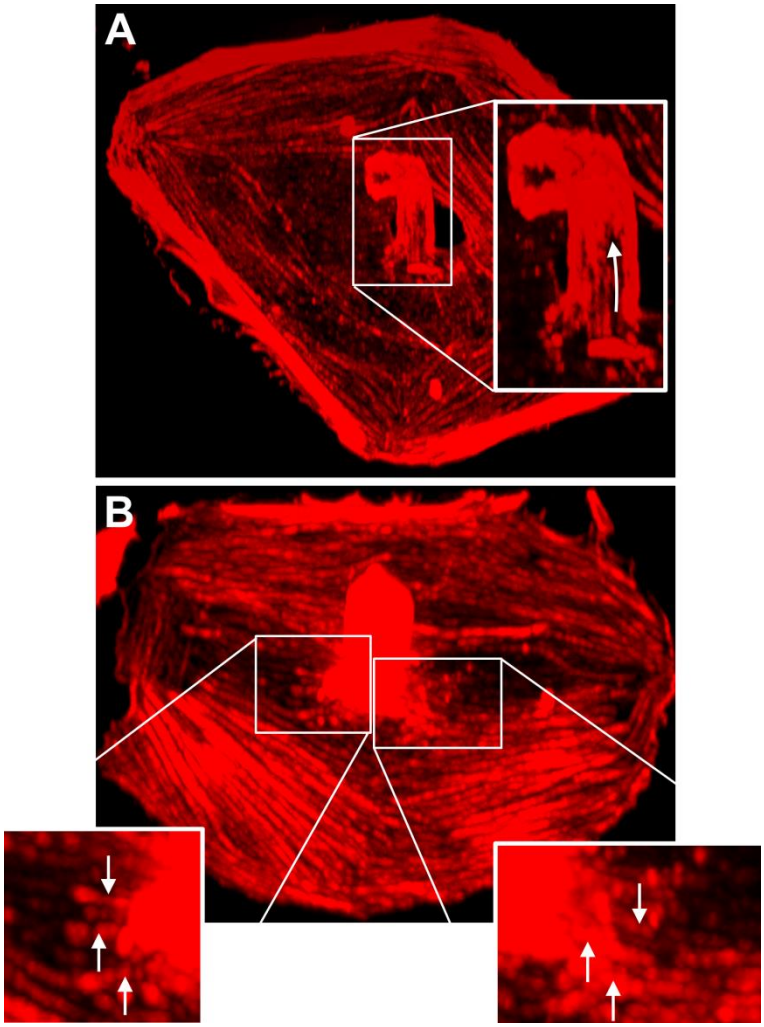

Figure 7: Out of plane 3D images of the actin cytoskeleton in aspirated cells. (A) Bands of SFs that extend along the aspirated portion of the cell are observed. The arrow in the zoomed-in inset image indicates the direction of the SFs. (B) SFs that extend from the base into the aspirated portion of the cell are indicated in zoomed-in inset images.

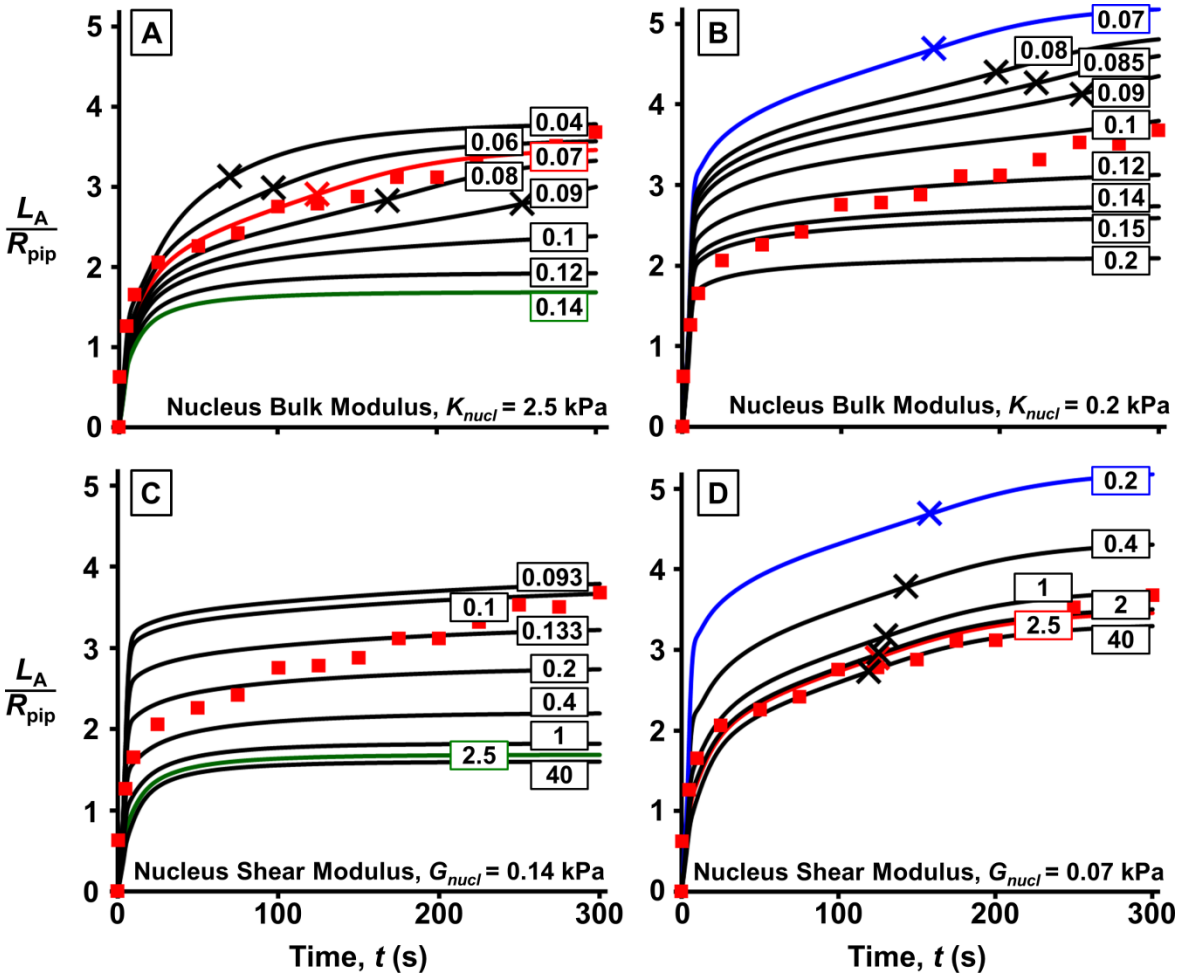

Figure 8: Parametric investigation of nucleus material properties. Active SF model is used to simulate the cell response to a 500 Pa applied pressure and different nucleus shear (G_{nucl}) and bulk (K_{nucl}) modulus values are considered. Normalised aspiration lengths as a function of time are shown and the 500 Pa experimental data is superimposed in all plots (red square data points) for direct comparison with computational results. (A) Shear modulus is varied between 0.04 kPa and 0.14 kPa, with a constant nucleus bulk modulus of 2.5 kPa. (B) Shear modulus is varied between 0.07 kPa and 0.2 kPa with a constant nucleus bulk modulus of 0.2 kPa. (C) Bulk modulus is varied between 0.093 kPa and 40 kPa, with a constant nucleus shear modulus of 0.14 kPa. (D) Bulk modulus is varied between 0.2 kPa and 40 kPa, with a constant nucleus shear modulus of 0.2 kPa. The curve that best fit the 500 Pa experimental data is indicated as the red solid line (found in (A) and (D)), with shear and bulk modulus values of 0.07 kPa and 2.5 kPa, respectively.

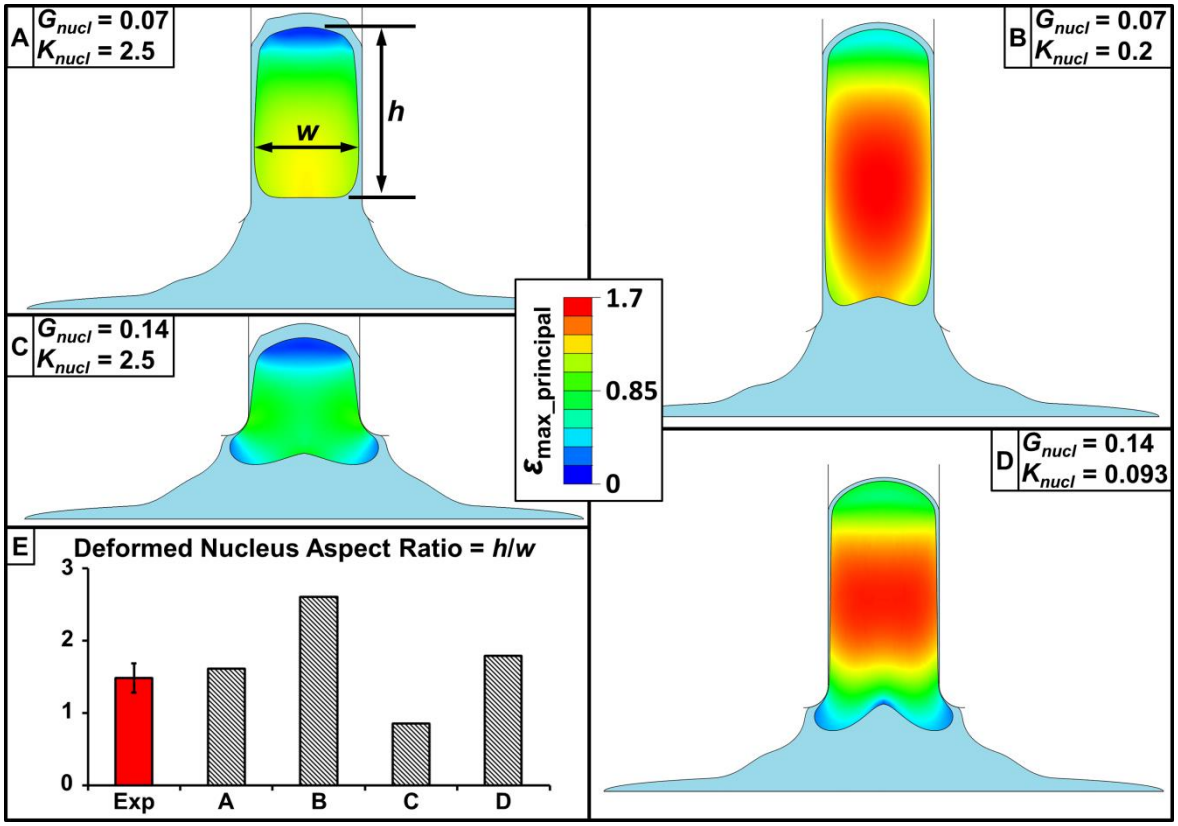

Figure 9: Using the active SF model in the cytoplasm, computed deformation is presented for cells in which different sets of nucleus shear (G_{nucl}) and bulk (K_{nucl}) modulus values are used. Associated normalised aspiration lengths can be found in Figure 8. The distribution of the computed maximum principal strain ($\varepsilon_{max\_principal}$) is shown in the deformed cell nuclei. Deformation is shown for simulations in which: (A) the best fit shear and bulk moduli are used in the nucleus (as indicated by the red curve in the nucleus parametric study presented in Figure 8); (B) the best fit shear modulus and a relatively low bulk modulus are used in the nucleus; (C) a relatively high shear modulus and the best fit bulk modulus are used in the nucleus; and (D) a relatively high shear modulus is used in the nucleus with a very low bulk modulus. (E) Experimentally (Exp) measured nucleus aspect ratio (mean ± standard deviation) and computed results for A-D above.